



RRDE experiments on noble-metal and noble-metal-free catalysts: Impact of loading on the activity and selectivity of oxygen reduction reaction in alkaline solution

Gaixia Zhang, Qiliang Wei, Xiaohua Yang, Ana C. Tavares ^{*}, Shuhui Sun ^{*}

Institut National de la Recherche Scientifique (INRS)-Énergie, Matériaux et Télécommunications, 1650 Boulevard Lionel-Boulet, Varennes, QC, J3X 1S2, Canada

ARTICLE INFO

Article history:

Received 25 August 2016

Received in revised form

28 December 2016

Accepted 2 January 2017

Available online 10 January 2017

Keywords:

Oxygen reduction reaction

Rotating ring-disk electrode

Catalyst loading

Hydrogen peroxide selectivity

Electron transfer number

ABSTRACT

Oxygen reduction reaction (ORR) is at the core of various applications, such as fuel cells, metal-air batteries and H_2O_2 electro-generation. Depending on the targeted application, catalysts that follow a “direct four-electron ($4e^-$)” pathway or “two-electron ($2e^-$)” pathway are envisaged. We have systematically investigated the impact of the electrocatalyst loading on the rotating ring-disk electrode (RRDE), on their activity and selectivity towards ORR in alkaline medium (0.1 M and 1 M KOH). Four representative catalysts, including a noble metal catalyst (commercial 20 wt% Pt/C, ETEK), metal-free catalysts (Printex carbon black and graphene), and non-noble metal catalyst (Fe/N/C), were selected because they exhibit different behaviours for ORR following a “direct four-electron ($4e^-$)” pathway, “two-electron ($2e^-$)” pathway, or a “series $2e^- + 2e^-$ ” pathway. The results confirmed that the catalyst loading influences the activity and the selectivity of the catalysts, with lower loadings favoring the H_2O_2 electrogeneration, and researchers should pay attention to it. Moreover, in order to make possible comparison between results coming from different research groups, we recommend reasonable loading ranges for each type of catalyst.

© 2017 Elsevier B.V. All rights reserved.

1. Introduction

From both fundamental and applied points of view, the oxygen reduction reaction (ORR) is one of the most important processes for various electrocatalysis applications, such as fuel cells [1–7], metal-air batteries [8–12] and H_2O_2 generation [13–15]. Nowadays, it is generally accepted that the ORR in aqueous solutions occurs mainly by three pathways summarized by three reactions, either in acid or alkaline, as shown in Table 1 [1,16]: a direct four electron ($4e^-$) reduction pathway from O_2 to H_2O , a two electron ($2e^-$) reduction pathway from O_2 to H_2O_2 , and a “series $2e^- + 2e^-$ ” pathway from O_2 to H_2O_2 and to H_2O . Since each of these pathways comprises multiple elementary steps, it must be kept in mind that such distinction offers only a macroscopic description of the overall reaction. In fuel cells, the desired route of oxygen reduction is the $4e^-$ pathway leading to H_2O formation. However, a $2e^-$ reduction to H_2O_2 can also occur, and the H_2O_2 becomes highly aggressive when it

breaks down into free radicals like OH^\bullet and OOH^\bullet . Therefore, minimizing the release of H_2O_2 is of great importance in the design of ORR electrocatalysts for fuel cells [17–19]. On the other hand, H_2O_2 is widely used in many industrial areas such as pulp bleaching and waste/drinking water treatment [20–22]. The only degradation product of its use is water and, thus, it is a very promising and safe oxidant for green chemistry. A promising approach to produce H_2O_2 is by electroreduction of O_2 in either acidic or alkaline media [15,23–25], which offers advantages including high purity, great safety, and low infrastructure investment and maintenance costs, as well as being environmentally friendly.

Half-cell testing has been extensively used as a characterization tool to determine the activity and selectivity of electrocatalysts to H_2O or H_2O_2 . The two main techniques commonly used are rotating disk electrode (RDE) and rotating ring-disk electrode (RRDE) tests, which have the great advantage of overcoming mass transfer limitation and thus evaluating kinetically controlled ORR activity [26–28]. In RDE, the catalyst activity can be directly observed and catalyst selectivity can be calculated using the Koutecky–Levich equation [13,29,30]. In RRDE, both catalyst activity and selectivity to H_2O and/or H_2O_2 formation can be directly obtained [25,31–33]. However, both RDE and RRDE techniques have recently

^{*} Corresponding authors.

E-mail addresses: tavares@emt.inrs.ca (A.C. Tavares), [\(S. Sun\).](mailto:shuhui@emt.inrs.ca)



Table 1
ORR pathways in acidic and alkaline solutions.

Medium	direct 4e ⁻ pathway	2e ⁻ pathway, or a sequential 4e ⁻ pathway
Acid	$O_2 + 4H^+ + 4e^- = 2H_2O$ (1)	$O_2 + 2H^+ + 2e^- = H_2O_2$ (3) $\longrightarrow H_2O_2 + 2H^+ + 2e^- = 2H_2O$ (5)
Alkaline	$O_2 + 2H_2O + 4e^- = 4OH^-$ (2)	$O_2 + H_2O + 2e^- = HO_2^- + OH^-$ (4) $\longrightarrow H_2O + HO_2^- + 2e^- = 3OH^-$ (6)

been questioned for the consistency of the selectivity results they provide, particularly with catalyst loading variances [34–39]. Few groups have presented evidence that the amount of detected H₂O₂ depends on the catalyst loading on the RRDE tip [34–36,39]. Especially, the Dahn's group [34–36] has reported on the impact of catalyst loading on the fraction of H₂O₂ release in acid medium, including (i) Fe/N/C catalyst, prepared by reaction of Sid Richardson carbon black and Fe precursors, (ii) Se/Ru/C catalyst, prepared using a wet chemical method, and (iii) 3M's nanostructured Pt thin film electrocatalyst. The observations indicate that lowering the catalyst loading led to a larger fraction of H₂O₂ formation. Does it mean that all catalysts show similar behaviour? Additional detailed studies on the effect of the catalyst loading are still needed, in order to unequivocally investigate and identify the ORR activity and selectivity of various catalysts.

In this work, we have investigated four representative catalysts for ORR which include a noble metal catalyst (commercial 20 wt% Pt/C ETEK), two metal-free catalysts (Printex carbon black and graphene), and a non-noble metal catalyst (MOF-based Fe/N/C, the most active non-noble metal catalyst for fuel cells reported so far). The catalyst loading on the RRDE electrode was varied, so that we can obtain a comprehensive idea about the effect of this parameter on the activity and selectivity for ORR. Those catalysts were chosen because they have different ORR behaviours following a 4e⁻ pathway, 2e⁻ pathway, or a “series 2e⁻ + 2e⁻” pathway. This work is focused on alkaline media (0.1 M and 1 M KOH), which is different from the previously reported work that mainly focused on acidic solution (pH value around 1). The results show that the catalyst loading on the working electrode is an important factor, even if different trends were found between catalysts. Further, based on the representative catalysts used in this work, recommended reasonable loading ranges to study each class of catalysts are also given.

2. Experimental

2.1. Syntheses of catalysts

Printex 6L carbon black was purchased from Evonik-Degussa, and 20 wt% Pt/C commercial catalyst was purchased from ETEK, and both were used as received. The graphene nanosheets were prepared using the procedure described in our previous paper [25]. In detail, 1 g of natural graphite powder was first stirred in 23 mL of concentrated H₂SO₄, followed by the addition of 0.5 g of NaNO₃ at room temperature. The stirring lasted for 16 h and after that the mixture was cooled down to 0 °C. Then, 3 g of KMnO₄ were added into the solution. After 2 h, a green slurry was formed at around 35 °C, which was then stirred for another 3 h. Then, 46 mL of H₂O was slowly added into the solution at around 98 °C. The suspension was kept at this temperature for 30 min before it was further diluted with another addition of water and 3 g of H₂O₂. The suspension was subsequently filtered and washed until reaching a neutral pH, then dried in a vacuum oven at 60 °C to obtain graphite oxide (GO). To obtain graphene, the as-synthesized GO was heated at around 1050 °C in Ar atmosphere for 2 min in a tube furnace.

For the synthesis of Fe/N/C catalyst, it was followed a similar procedure reported the Dodelet's group [40]. That is, 1600 mg of

a metal organic framework (MOF) of zeolitic imidazolate framework (ZIF-8), 400 mg of 1,10-Phenanthroline, and 64 mg of iron(II) acetate were first mixed for 2 h at room temperature in 100 mL of ethanol and 20 mL of de-ionized (DI) water (18.2 MΩ cm, Sartorius Arium Water Purification Systems). Then the mixture was heated to 60–80 °C for 2–3 h until about 50 mL of thick slurry was obtained. The slurry was placed in a drying oven at 95 °C and in air where it was left overnight. The resulting dry powder was then transferred under N₂ in a 65 cm³ steel vial containing 20 chrome-steel balls of 0.25 inch diameter. After sealing the vial under N₂, it was placed in a planetary ball-miller (Pulverisette 7, Fritsch) to go through a 3 h ball-milling step at 400 rpm. The ball-milled powder was then pyrolyzed in Ar at 1050 °C for 1 h until a weight loss of about 70% was obtained, and then in pure NH₃ at 950 °C until a subsequent 50% weight loss was obtained.

2.2. Transmission electron microscopy and specific surface area characterizations

The morphology of the four samples was characterized using a JEOL 2100 F transmission electron microscope (TEM) at an acceleration voltage of 200 kV. Adsorption and desorption isotherms were measured at 77 K using nitrogen as adsorbate down to relative pressure P/P₀ 1 × 10⁻⁶ with Quantachrome Instrument. The samples were weighed, placed on the analysis port, and prior to analysis they were heated at 200 °C for 2 h under vacuum. The adsorption data was analyzed using the Brunauer–Emmett–Teller (BET) theory and for the pore size distribution the quenched solid density functional theory (QSDFT) was used, assuming pores with a slit-like structure. Autosorb-1 Software from Quantachrome Instrument was used to elaborate the data.

2.3. Rotating ring disk electrode measurements

The activity of the catalysts towards ORR, the number of electrons transferred during ORR, and the percentage of peroxide produced by the reaction were evaluated for each catalyst by RRDE measurements. The diameter of the glassy carbon disk is 5.61 mm. It is surrounded by a Pt ring (6.25 and 7.92 mm inner and outer diameters, respectively).

2.3.1. Ink formulations

For the noble metal catalyst, i.e., 20 wt% Pt/C, the catalyst ink was prepared according to the following formulation: 5 mg of catalyst were dispersed ultrasonically in 85 μL of deionized water, 1650 μL of ethanol and 50 μL of 5 wt% Nafion® perfluorinated resin solution (Aldrich). A series of different volumes (0.25, 1, 5, 9, and 45 μL) of ink were deposited on a 0.2475 cm² glassy carbon disk, resulting in catalyst loadings of 0.6, 2.3, 11.3, 20.4, and 101.9 μg_{Pt} cm⁻², respectively. For all non-noble metal and metal free catalysts, the following ink formulation was used: 10 mg of catalyst were added to 350 μL of ethanol and 95 μL of 5 wt% Nafion® perfluorinated resin solution. A series of different volumes (1, 5, 9, 12, and 15 μL) of ink are deposited on the glassy carbon disk, resulting in catalyst loadings of 90.8, 453.9, 817.1, 1089.5, and 1361.8 μg cm⁻², respectively. For Fe/N/C catalyst, due to its high activity and high surface area, two additional loadings of 9.1 and 22.7 μg cm⁻² were evaluated.

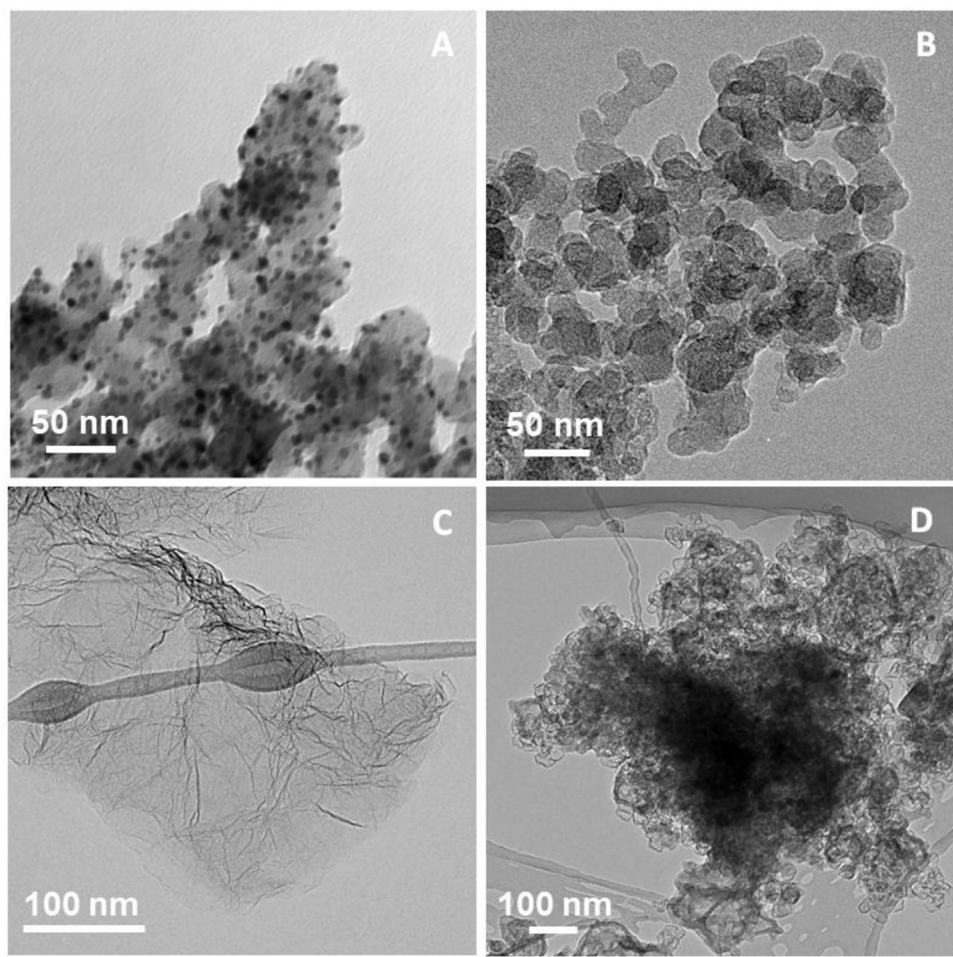


Fig. 1. TEM images of (A) 20 wt% Pt/C (ETEK), (B) Printex 6L carbon black, (C) graphene, and (D) Fe/N/C catalysts.

2.3.2. Measurements in O_2 - and N_2 -saturated electrolytes

The RRDE measurements were performed at room temperature in a three-electrode single compartment cell containing 0.1 M or 1 M KOH solution. The linear sweep voltammograms (LSVs) were recorded at 10 mV s^{-1} between -1.10 and 0.25 V vs. SCE with a Pine potentiostat (model AFRDE4), under N_2 - or O_2 -saturated electrolytes. The ring electrode was held at 1.3 V vs Reversible Hydrogen Electrode (RHE) during the ORR measurements, and the RRDE rotation rate was set at 1600 rpm. The net Faradic current was obtained by subtracting the voltammogram recorded under N_2 from the one recorded under O_2 . All currents presented in the figures are Faradic current. For noble metal catalyst, prior to the ORR activity measurement, a clean procedure is needed to activate the catalyst; that is, about 20 cycles cyclic voltammetry (CV) scans at 50 mV s^{-1} in N_2 -saturated electrolyte was performed until steady-state voltammograms were obtained.

The equations used to calculate n (the apparent number of electrons transferred during ORR) and $\%H_2O_2$ (the percentage of H_2O_2 released during ORR) are the following:

$$n = \frac{4I_D}{I_D + I_R/N} \quad (7)$$

$$\%H_2O_2 = 100 * \frac{2I_R/N}{I_D + I_R/N} \quad (8)$$

where I_D is the current at the disk, I_R is the current at the ring and N (calculated value is 0.37) is the RRDE collection efficiency. Empirical measurements of collection efficiency were conducted in 1 M KNO_3 and 10 mM $K_3Fe(CN)_6$ (Aldrich, >99%) deaerated with pure nitrogen (Praxair, N5.0). The CV scans were recorded at 10 mV/s between 0.0 V and 1.0 V vs. RHE at 1600 rpm, while the ring was kept at 1.55 V vs. RHE to re-oxidize the ferrocyanide produced at the disk. For the working electrodes with different catalysts and loadings,

Table 2

Summary of the performance indicators of Pt/C at 1600 rpm for ORR in 0.1 M KOH solution, with various catalyst loadings on RRDE tips.

Pt/C loading on RRDE ($\mu\text{g}_{\text{Pt}} \text{ cm}^{-2}$)	Diffusion-limited current density (mA cm^{-2})	Half-wave potential (V vs RHE)	Onset potential (V vs RHE)	$\%H_2O_2^a$	n^a
0.6	4.2	0.69	0.88	7.2	3.85
2.3	5.5	0.78	0.92	0.6	3.99
11.3	5.5	0.85	0.97	0.6	3.99
20.4	5.5	0.86	0.98	0.6	3.99
101.9	5.5	0.89	1.04	0.6	3.99

^a $\%H_2O_2$, and n read at 0.3 V vs RHE.

CVs were also recorded in 1 M KNO₃ at the same scan rate, in order to remove the background (non-Faradaic current) from the curve obtained with K₃Fe(CN)₆ electrolyte. After background subtraction, both anodic and cathodic limiting currents were obtained, and the collection efficiency can be expressed as a positive number from the following equation.

$$N_{\text{empirical}} = (-I_{\text{Ring,limiting}}/I_{\text{Disk,limiting}}) * 100\% \quad (9)$$

The collection efficiency values are reported in Fig. S1. Basically, for each catalyst the collection efficiency is fairly independent of the catalyst loading. For Pt/C, graphene, and Fe/N/C used in this work, the measured collection efficiency (i.e. 37% ± 1.5%) is similar to the calculated value (based on the RRDE geometry) given by the Pine manufacturer, considering the experimental error range. However, for Printex, a slightly higher collection efficiency was obtained (ca. 40%), which was attributed to the aggregation (non-uniform deposition) of the Printex on the working electrode, causing a more turbulent electrolyte flow.

3. Results and discussion

3.1. Noble metal catalyst in 0.1 M KOH: commercial 20 wt% Pt/C

Commercial ETEK 20 wt% Pt/C catalyst was selected as the representative noble metal catalyst since it is quite commonly used as standard reference catalyst in various studies. Its morphology is shown in Fig. 1A. Fig. 2A and B presents the current densities of disk and ring versus disk potential for 20 wt% Pt/C with different catalyst loadings of 0.6, 2.3, 11.3, 20.4, and 101.9 μg_{Pt} cm⁻² on the RRDE tip in 0.1 M KOH solution. All curves show the same typical shape of Pt catalysts, but the ORR activity (e.g., onset potential (E_{on}) and half-wave potential ($E_{1/2}$)) is significantly improved with increas-

ing the catalyst loading. Herein, E_{on} is defined as the potential corresponding to a current density of 0.1 mA cm⁻² in a steady-state RRDE experiment [41] and $E_{1/2}$ is the potential at which the polarization curve current is equal to one half of diffusion current. Table 2 summarizes the performance indicators of Pt/C at various catalyst loadings in 0.1 M KOH, including the diffusion-limited current density, half-wave potential and onset potential, as well as hydrogen peroxide selectivity (%H₂O₂) and the number of electron transferred (n) at a representative disk potential of 0.3 V vs RHE. The diffusion-limited current for a perfect smooth disk electrode rotating with an angular velocity of ω , is expressed by the Levich equation [13,29,30]:

$$I_d = 0.62nFSD_{O_2}^{2/3}v^{-1/6}\omega^{1/2}C_{O_2} \quad (10)$$

where n , F , D , v , ω , C , and S refer to the number of electrons transferred in ORR (mol⁻¹), Faraday's constant (C mol⁻¹), diffusion coefficient of the analyte (cm² s⁻¹), kinematic viscosity of the electrolyte (cm² s⁻¹), angular velocity of the rotating electrode (rad s⁻¹), concentration of the analyte (mol cm⁻³), and "effective electrode area" (cm²). For most of the loading levels (except of 0.6 μg_{Pt} cm⁻², which will be discussed later), a diffusion-limited current density close to the theoretical value is achieved (5.5 mA cm⁻² at 1600 rpm for the 4e⁻ reduction of oxygen [29], Eq. (10)). This is confirmed by the values of %H₂O₂ and n as a function of the disk potential, shown in Fig. 2C and D, mostly %H₂O₂ < 1 and n > 3.98 regardless of the catalyst loadings, demonstrating a direct 4e⁻ reduction process for Pt/C catalyst. The very tiny "upturn" in the disk reduction current which commences at more negative disk potential, coinciding with an increased yield of H₂O₂ vs potential, is due to the hydrogen under potential deposition (H_{upd}) on the Pt surface. When the catalyst loading is very low, such as 0.6 μg_{Pt} cm⁻², the Pt/C shows lower ORR activity, higher

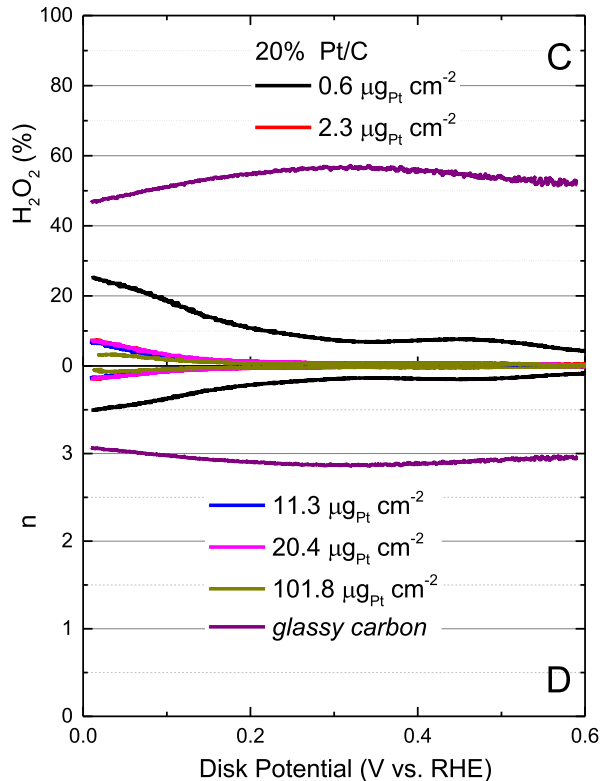
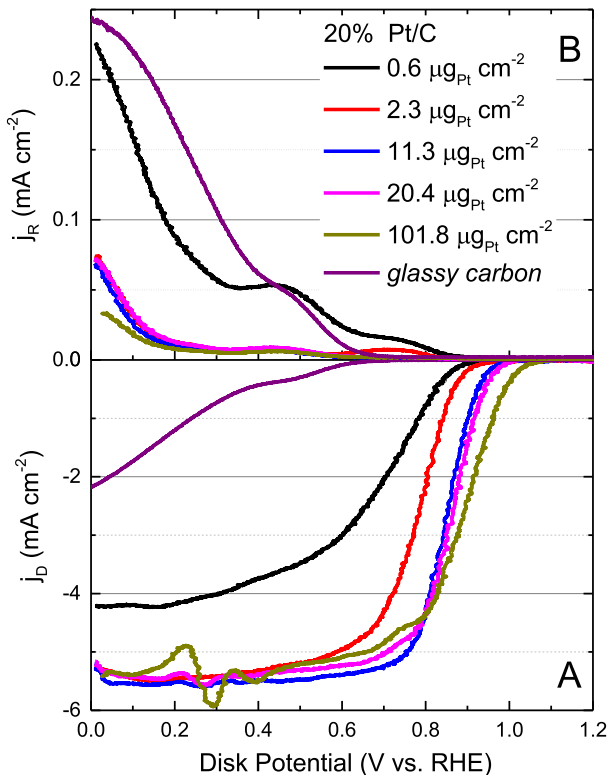


Fig. 2. (A) Typical polarization curves of the disk electrode and (B) the ring current density, as well as (C) the selectivity (%H₂O₂) and (D) the number of electron transferred, as a function of the disk potential for various 20 wt% Pt/C (ETEK) catalyst loadings, at 1600 rpm in 0.1 M KOH solution. Note that the determination of %H₂O₂ and n for potentials more positive than 0.6 V vs RHE is not shown because the disk and ring currents become too small at that range, resulting in large errors. (For interpretation of the references to colour in this figure legend, the reader is referred to the web version of this article.)

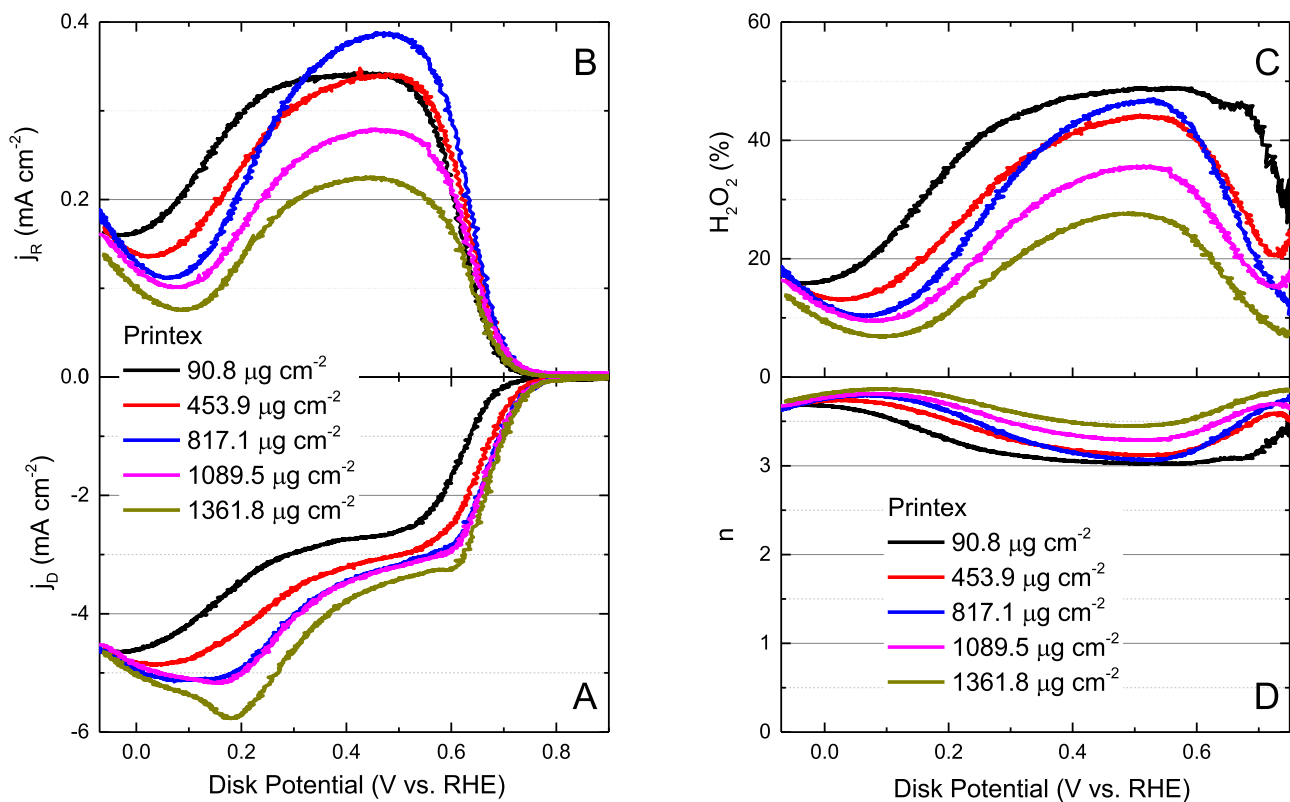


Fig. 3. (A) Disk and (B) ring current densities, as well as (C) the selectivity ($\% \text{H}_2\text{O}_2$) and (D) the number of electron transferred, as a function of the disk potential for various Printex catalyst loadings, at 1600 rpm in 0.1 M KOH solution. (For interpretation of the references to colour in this figure legend, the reader is referred to the web version of this article.)

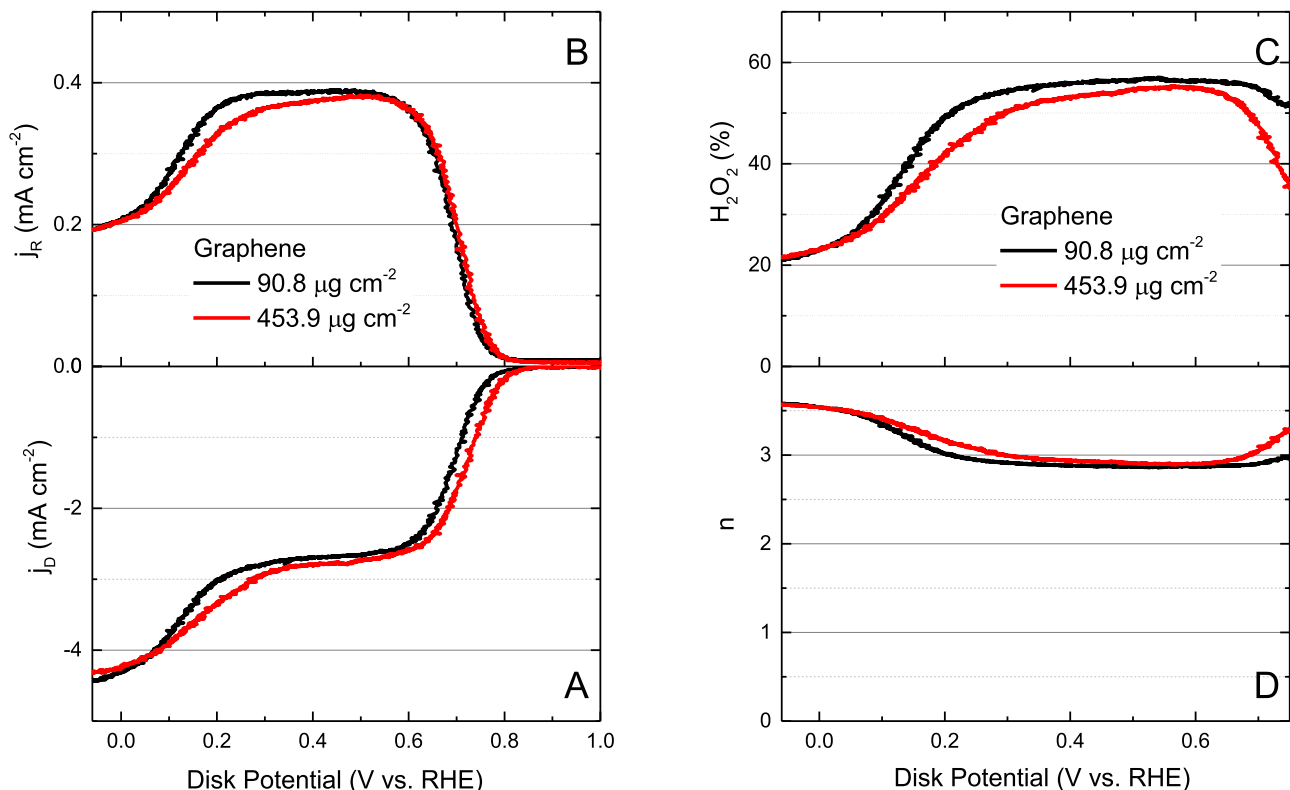


Fig. 4. (A) Disk and (B) ring current densities, as well as (C) the selectivity ($\% \text{H}_2\text{O}_2$) and (D) the number of electron transferred, as a function of the disk potential for various graphene catalyst loadings, at 1600 rpm in 0.1 M KOH solution. (For interpretation of the references to colour in this figure legend, the reader is referred to the web version of this article.)

Table 3

Textural properties of each catalyst.

Calculation model	BET	QSDFT ^a porosity measurements ($\text{m}^2 \text{ g}^{-1}$)		
Mechanism	Complete monolayer	Micropore filling		
P/P ₀ range	0.01–0.30	10 ^{–6} –1		
Samples	BET ($\text{m}^2 \text{ g}^{-1}$) ^c	Total ^b surface area	Micropore Surface area	Mesopore surface area
20 wt% Pt/C	87	109	42	67
Printex 6L carbon	243	270	207	63
Graphene	560	632	0	632
Fe/N/C	681	731	626	105

^a Quenched solid density functional theory (QSDFT) is an advanced DFT method for the pore size analysis of geometrically and chemically disordered micro-mesoporous carbons, which allows the calculation of pore size distributions from ca. 0.6 nm up to 34 nm.

^b The total surface area obtained by QSDFT is equal to the micropore surface area plus the mesopore surface area.

^c Due to the different calculation models, the value of BET surface area (based on monolayer adsorption which does not necessarily apply to microporous materials) will not be the same value as calculated by DFT (based on micropore filling). For micropore materials, most of the times, the BET surface area is smaller than the DFT surface area.

% H_2O_2 , and lower diffusion-limited current density, compared to the results with higher catalyst loadings. That is, when the catalyst layer is very thin, the produced H_2O_2 at the catalyst active site will quickly escape and is easily caught by the Pt ring, rather than to be further reduced to H_2O on the disk. Obviously, with decreasing catalyst loading, the thickness of the catalyst layer is decreased. At very low loading, such as 0.6 $\mu\text{g}_{\text{Pt}} \text{ cm}^{-2}$, in fact, the catalyst could not cover the entire surface of the RRDE tip. This therefore gives another possible reason for the diffusion-limited current density with a value lower than the theoretical one. It is worth to note that simply to regard S as RRDE electrode area (geometric area of the disk electrode, named as A) will not give a precise answer to match the experimental data. In the case of a very low catalyst loading, the real effective area of the catalyst (active site area) will be smaller than the geometric area A , resulting in a lower value of the diffusion-limited current than the one calculated using the geometric area A (shown in Fig. 2A). In this situation, the ORR activity is governed by both the electrocatalyst and the glassy carbon. As we know, most of

the time, the catalysts reported by the researchers are more active than the glassy carbon. Still, in order to neglect the contribution of the glassy carbon from RDE/RRDE tip, one has to make sure that the amount of the catalyst will be enough to cover the entire working area of the electrode. On the other hand, when the catalyst loading is very high, it is difficult to avoid bumping or dry-muddy like covering. Thus, turbulence/vortex formation occurs, resulting in single waves in the disk reduction current (Fig. 2A with catalyst loading of 101.9 $\mu\text{g}_{\text{Pt}} \text{ cm}^{-2}$). Therefore, in order to make better comparison among different research groups, a representative Pt loading range of 10–20 $\mu\text{g}_{\text{Pt}} \text{ cm}^{-2}$ is recommended. Fig. S1 shows the Tafel analysis of 20 wt% Pt/C catalyst. For the Tafel plot, the kinetic current was calculated after mass-transport correction according to the following equation [42]:

$$\frac{1}{j} = \frac{1}{j_K} + \frac{1}{j_L} \Rightarrow j_K = \left| \frac{j * j_L}{j - j_L} \right| \quad (11)$$

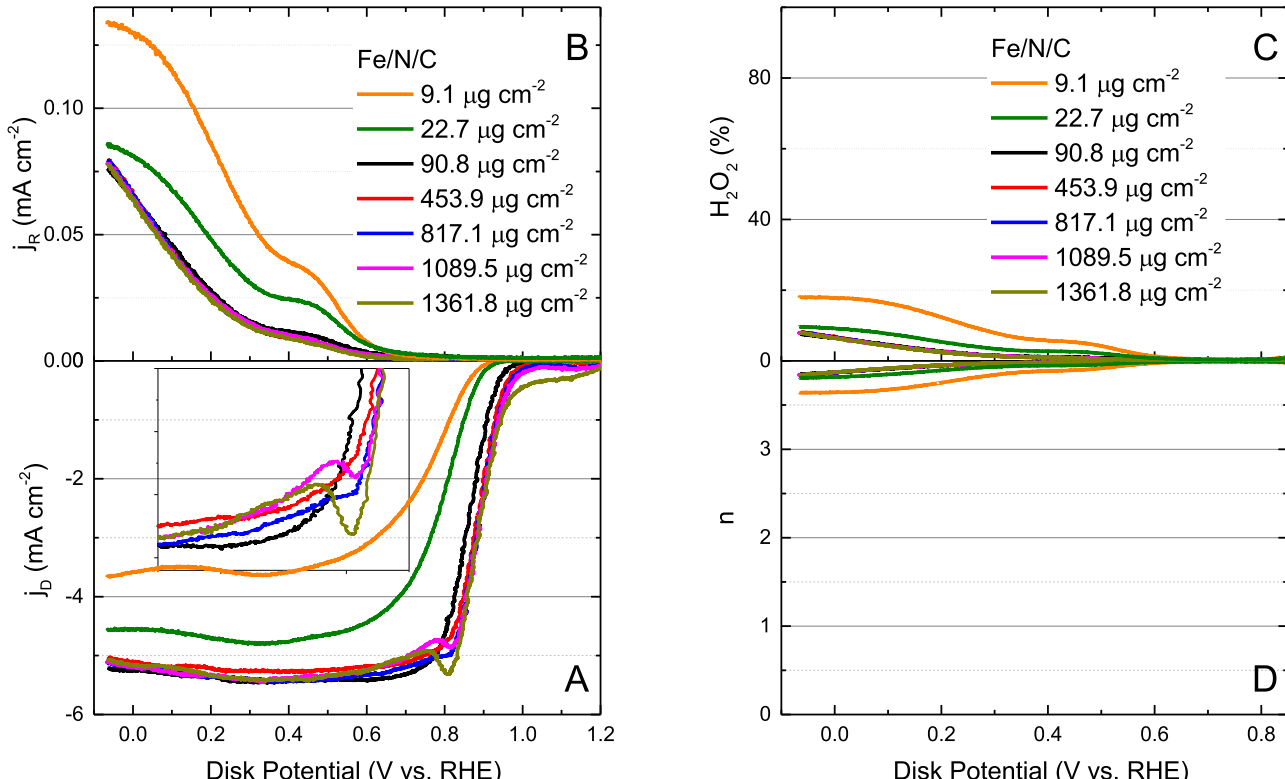


Fig. 5. (A) Disk and (B) ring current densities, as well as (C) the selectivity (% H_2O_2) and (D) the number of electron transferred, as a function of the disk potential for various Fe/N/C catalyst loadings, at 1600 rpm in 0.1 M KOH solution. (For interpretation of the references to colour in this figure legend, the reader is referred to the web version of this article.)

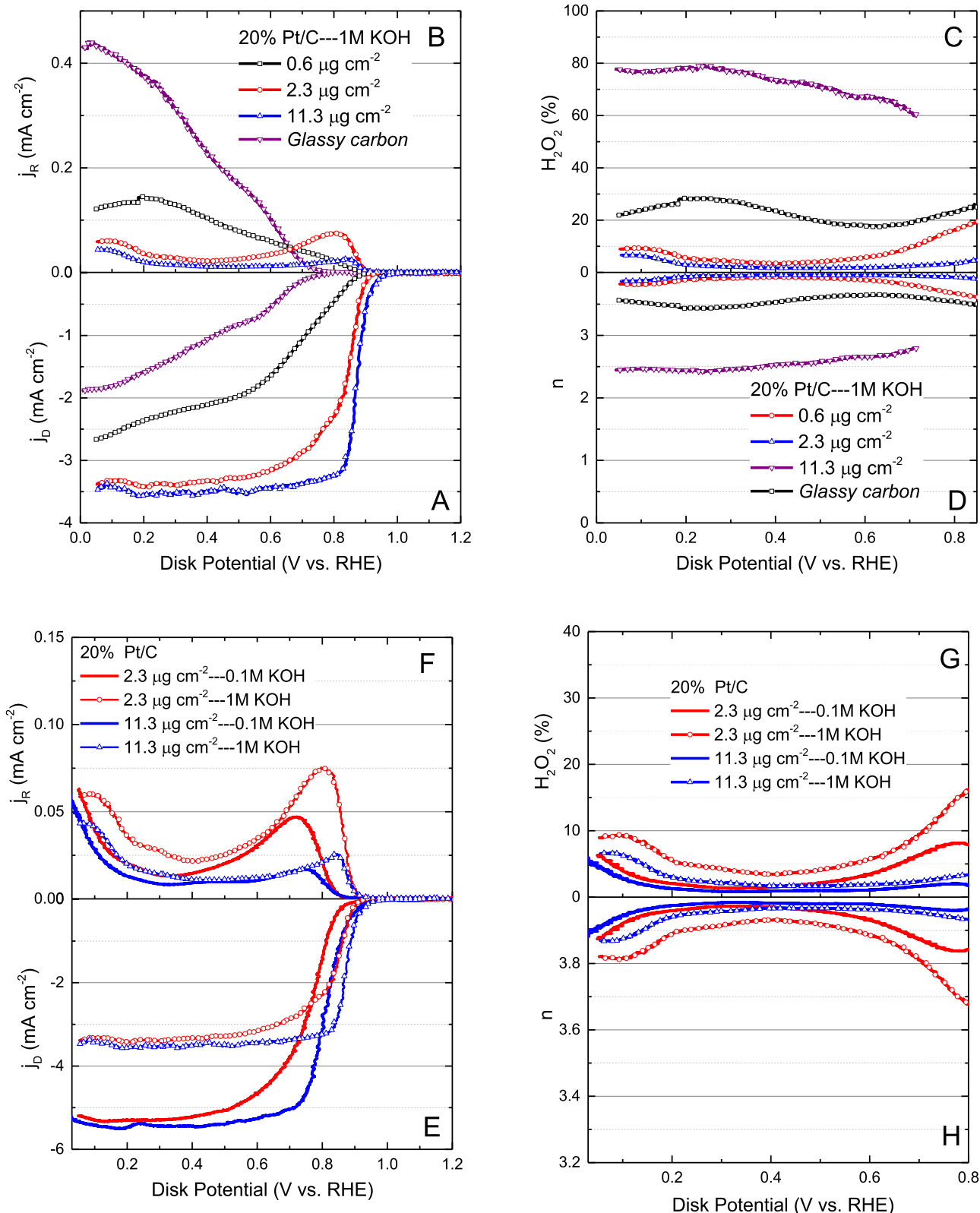


Fig. 6. (A) Disk and (B) ring current densities, as well as (C) $\% \text{H}_2\text{O}_2$ and (D) n , as a function of the disk potential for various 20 wt% Pt/C (ETEK) catalyst loadings, at 1600 rpm in 1 M KOH solution. (E–H) the comparison of ORR behaviour of Pt/C, with two representative catalyst loadings (2.3 and $11.3 \mu\text{g}_{\text{Pt}} \text{cm}^{-2}$), at 1600 rpm in 0.1 M and 1 M KOH solutions respectively. (For interpretation of the references to colour in this figure legend, the reader is referred to the web version of this article.)

The Tafel slope of Pt/C with different catalyst loadings waves in the range of 60 – $70 \text{ mV decade}^{-1}$, in good agreement with the most of the values reported in the literature. Moreover, if the Tafel plots were draw in terms of the mass activity, as shown in Fig.

S2B, all curves overlap except for the one with the highest loading ($101.9 \mu\text{g}_{\text{Pt}} \text{cm}^{-2}$). This shows that an excessive loading blocks the usage of the catalyst. The constancy of Tafel slopes values demon-

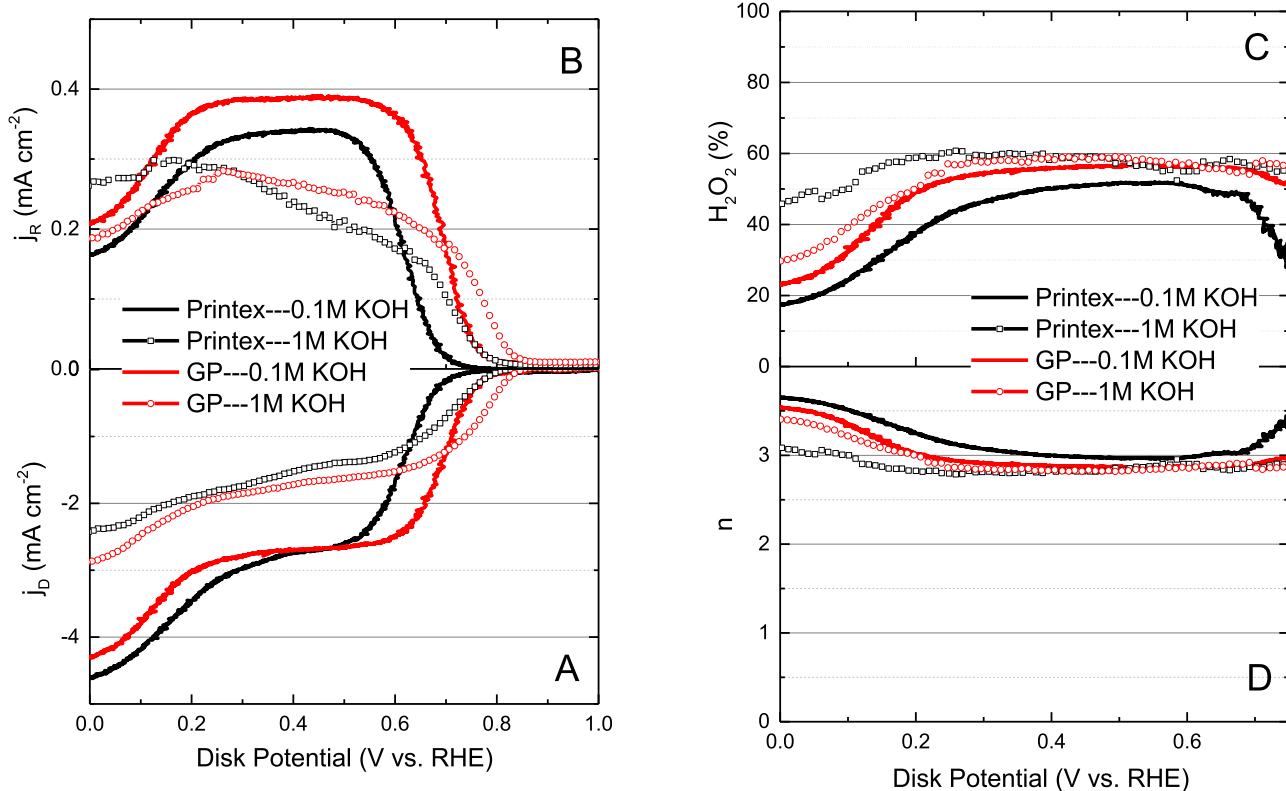


Fig. 7. (A) Disk and (B) ring current densities, as well as (C) the selectivity ($\% \text{H}_2\text{O}_2$) and (D) the number of electron transferred, as a function of the disk potential for Printex and graphene with a catalyst loading of $90.8 \mu\text{g cm}^{-2}$, at 1600 rpm in 0.1 M and 1 M KOH solutions respectively. (For interpretation of the references to colour in this figure legend, the reader is referred to the web version of this article.)

strates that the loading does not affect the kinetics of the ORR reaction.

3.2. Metal-free catalysts in 0.1 M KOH: Printex 6L carbon and graphene

Recently, a new class of metal-free ORR catalyst based on carbon nanomaterials has been discovered, which as alternative ORR catalysts, could dramatically reduce the cost and increase the efficiency of oxygen reduction. It is also well known that carbon materials are excellent catalysts for H_2O_2 generation in alkaline medium. Therefore, in this work, we selected Printex 6L carbon and graphene as the two representative carbon materials for the study of loading effect of metal-free catalysts on ORR (Fig. 3 and 4). Again, with increasing the catalyst loading, the ORR activity is increased, which is consistent with the results of Pt/C catalyst. However, there is an obvious ORR shape difference between Printex, graphene and Pt/C catalysts. Printex and graphene have two oxidation reduction waves, meaning that ORR does not follow either 2e^- or 4e^- pathway; this contrasts with Pt/C that shows only one reduction wave and follows a direct 4e^- pathway. Detailed analysis of Figs. 3 C/4C and 3D/4D, shows a much higher H_2O_2 yield for Printex and graphene (20%–60%) than for Pt/C, in a large range of disk potential (0.2–0.8 V vs. RHE). Comparing the results of Printex and graphene (Figs. 3C/D and 4C/D), we can see that graphene has much longer range of 2e^- reduction process. The values of $\% \text{H}_2\text{O}_2$ and n change with the disk potential, and this illustrates the advantage of RRDE measurements over RDE, since with the former it is possible to extract directly and *in-situ* the values of $\% \text{H}_2\text{O}_2$ and n as a function of potential from linear scan voltammograms recorded at one single rotation rate. RRDE measurements are therefore very convenient when the disk currents do not level off (as shown in Fig. 3A for Printex carbon), as often observed in the case for non-noble metal based catalysts.

The diffusion-limited current density for Printex increases with increasing the catalyst loading. However, with the highest catalyst loadings such as 1089.5 and $1361.8 \mu\text{g cm}^{-2}$, the ORR currents still have difficulty to reach the diffusion limiting plateau. The thickness of the catalyst layer is closely related not only to the catalyst loading but also to the volume density (or surface area) of the catalyst. Table 3 summarizes the specific surface areas for these four representative catalysts. The N_2 adsorption/desorption isotherms and pore volume distribution of the catalysts are shown in Fig. S3. The specific surface area of the Printex is $230 \text{ m}^2 \text{ g}^{-1}$, and it is difficult to form a uniform catalyst layer on entire RRDE tip surface because this carbon black aggregates easily before the ink is dried. With increasing the catalyst loading, the electrode changes from sparsely distributed catalyst to almost a fully covered electrode. Thus, the previous hypothesis that a smaller S resulted in lower diffusion-limited current, is also applicable to Printex carbon.

The graphene sample used in this work has a specific surface area of $560 \text{ m}^2 \text{ g}^{-1}$, about 2 times higher than that of Printex carbon, with a very low volume density. Thus, the graphene ink solution was quite thick and the catalyst layers were uniform. Consequently, with higher graphene loading (817.1, 1089.5, and $1361.8 \mu\text{g cm}^{-2}$), it was difficult to finish all the tests because some graphene drops off from the electrode. Therefore, only two loadings (90.8 and $453.9 \mu\text{g cm}^{-2}$) were evaluated. Compared to Printex, graphene has a much higher ORR activity (at -0.3 V with catalyst loading of $453.9 \mu\text{g cm}^{-2}$, 1.67 mA cm^{-2} for graphene vs 0.51 mA cm^{-2} for Printex), and a wider potential range for the first reduction step. With increasing catalyst loading, the ORR activity is increased, but, the ORR curves reach almost the same limiting current plateau. This confirms that when the electrode's surface is fully covered by the catalyst, catalyst loading does not affect the value of the diffusion-limited current. However, it does affect the $\% \text{H}_2\text{O}_2$ and n (shown in Fig. 4C and D), i.e., the higher catalyst loading, the lower is $\% \text{H}_2\text{O}_2$.

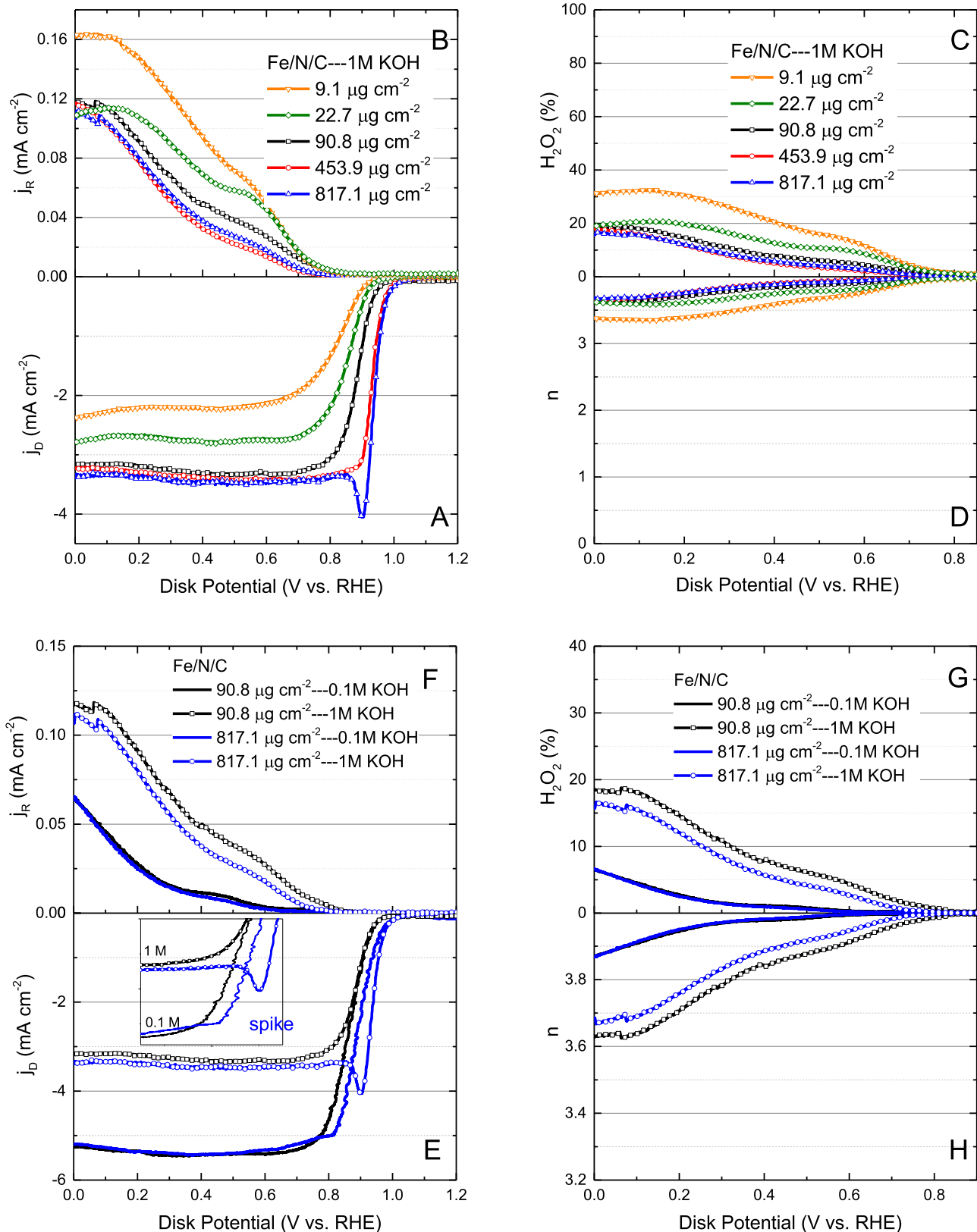


Fig. 8. (A) Disk and (B) ring current densities, as well as (C) $\% \text{H}_2\text{O}_2$ and (D) n , as a function of the disk potential for different $\text{Fe}/\text{N}/\text{C}$ catalyst loadings, at 1600 rpm in 1 M KOH solution. (E–H) the comparison of ORR behaviour of $\text{Fe}/\text{N}/\text{C}$, with two representative catalyst loadings (90.8 and $817.1 \mu\text{g cm}^{-2}$), at 1600 rpm in 0.1 M and 1 M KOH solutions respectively. (For interpretation of the references to colour in this figure legend, the reader is referred to the web version of this article.)

produced and the higher is n . This can be explained by the internal diffusion effect: for a thick catalyst layer, the produced H_2O_2 is not able to escape promptly the disk electrode to be caught by

the Pt ring, and is further reduced to OH^- . In addition, the loading effect is more obviously seen in Printex carbon than in graphene because, when the catalyst could not fully cover the electrode sur-

face, the $\%H_2O_2$ will be more affected by the effective area than the catalyst loading. Therefore, for better comparison among different research groups, a representative loading range of metal-free catalyst is suggested, i.e., 400–800 $\mu\text{g cm}^{-2}$ for Printex type, and 400–800 $\mu\text{g cm}^{-2}$ for graphene type. More precise and narrower loading range will depend on the specific surface area and surface chemistry of the catalyst. Thus, for each new material, it is highly recommended to investigate the catalyst loading effect on the ORR, to determine the optimum catalyst loading and to fully understand its electrochemical properties.

3.3. Non-noble metal catalysts in 0.1 M KOH: Fe/N/C

Fig. 5 shows the results of similar measurements for MOF-based Fe/N/C catalyst. This is so far one of the most active ORR catalysts and is able to display power densities comparable to those of the commercial Pt/C catalyst. Interestingly, under the same loading range as the metal free catalysts (90.8–1361.8 $\mu\text{g cm}^{-2}$), this catalyst shows similar activity and diffusion-limited current density for all investigated loadings. In fact, this catalyst is highly active and also has a very high specific surface area of $731\text{ m}^2\text{ g}^{-1}$, thus even with a low loading of 90.8 $\mu\text{g cm}^{-2}$, the catalyst can spread uniformly on the entire electrode surface, thus resulting in the same and expected value of diffusion-limited current density. Still, the catalyst activity slightly increases with increasing loading, which is consistent with the other catalysts (Pt/C, Printex, and graphene). However, there is no obvious effect of the loading on the $\%H_2O_2$ and n (almost invariant), as shown in Fig. 5C and D. This indicates that this type of Fe/N/C catalyst indeed follows a direct 4 e^- transfer process. It is important to note that this result may not be valid for all the Fe-based non-noble catalyst; therefore, an investigation on the loading effect is still recommended for the newly developed catalysts. In order to confirm our hypothesis that very low loading affects the value of S and then the diffusion-limited current, two additional loadings of 9.1 and 22.7 $\mu\text{g cm}^{-2}$ of Fe/N/C catalyst were also tested in 0.1 M KOH. As expected, a much lower diffusion-limited current density (3.6 and 4.8 mA cm^{-2} , vs 5.5 mA cm^{-2}) and a slightly higher $\%H_2O_2$ (9% and 18%, vs 6% at 0 V vs RHE) than that of the other loadings were determined, a phenomenon very similar to the Pt/C catalyst. On the other hand, for catalyst loadings equal or higher than 817.1 $\mu\text{g cm}^{-2}$, a spike (peak current density) appears at 0.8 V vs RHE, right before the diffusion-limited current plateau; the higher the catalyst loading, the larger is the observed current spike. This is associated with the adsorption rate of oxygen species on the catalyst active sites, i.e., thicker catalyst layer (by higher loading), longer time is needed for oxygen to diffuse and to reach all the active sites. This spike also brings some drawbacks such as to make the Tafel analysis. Therefore, to avoid the appearance of this spike, a suggested loading range for this type of catalyst is 400–800 $\mu\text{g cm}^{-2}$, depending on the surface area/volume density of the catalyst.

3.4. Additional study of ORR in 1 M KOH

Previous studies on nitrogen doped carbon nanotubes showed that the number of exchanged electrons n decreases with increasing KOH concentration [43]. Thus, ORR studies were also carried out in 1 M KOH. Fig. 6A–D shows the results of 20 wt% Pt/C with three representative loadings (0.6, 2.3 and 11.3 $\mu\text{g}_{\text{Pt}}\text{ cm}^{-2}$). It can be seen that all the curves in 1 M KOH keep the same shape as those of 0.1 M KOH, and the trend with the catalyst loading is the same as well. When the ORR curves recorded in different KOH solutions are compared in the same figure, it shows that increasing the KOH concentration results in (i) a positive shift of the ORR onset potential, (ii) a decrease of the diffusion-limited current density from 5.5 mA cm^{-2} (0.1 M KOH) to 3.5 mA cm^{-2} (1 M KOH), (iii) a slight

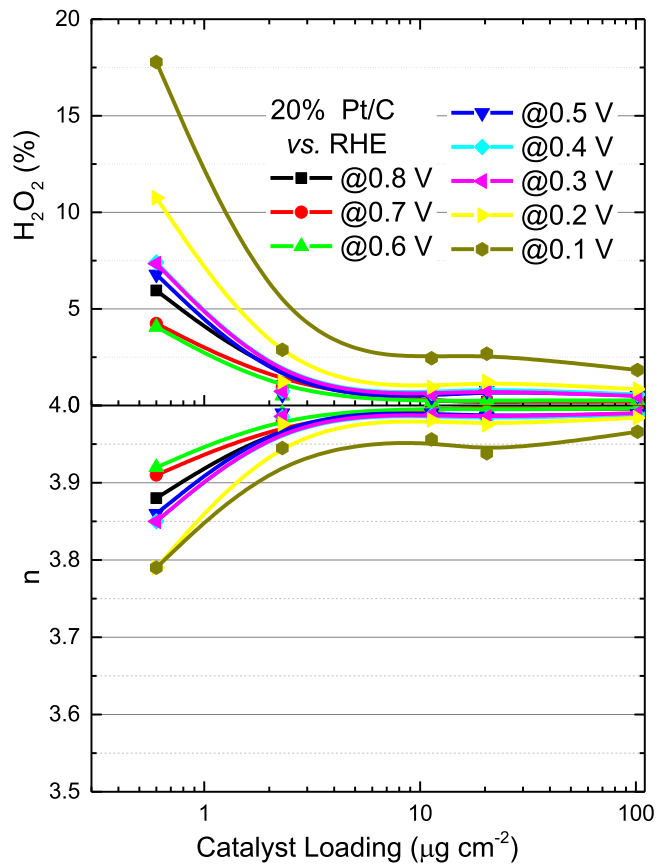


Fig. 9. Variation of the selectivity ($\%H_2O_2$) and the number of electron transferred, for 20 wt% Pt/C catalyst, as a function of the catalyst loading on RRDE, under different disk potentials, at 1600 rpm in 0.1 M KOH solution. (For interpretation of the references to colour in this figure legend, the reader is referred to the web version of this article.)

increase of $\%H_2O_2$ (from 1.8% to 3.6%, at 0.3 V vs RHE) and consequent decrease of n (from 3.97 to 3.93, at 0.3 V vs RHE). This is due to the lower O_2 solubility (7.8×10^{-7} vs 1.2×10^{-6} mol cm^{-3}) and lower O_2 diffusion coefficient (1.8×10^{-5} vs 1.9×10^{-5} $\text{cm}^2\text{ s}^{-1}$) in 1 M vs. 0.1 M KOH, while the values of the kinematic viscosity of the two solutions are same ($0.01\text{ cm}^2\text{ s}^{-1}$) [44,45]. On the other hand, with decreasing the catalyst loading (Fig. 6E–H), the difference between the $\%H_2O_2$ obtained in 1 M and 0.1 M KOH solutions increases (i.e., $\Delta = 0.97\%$ (1.81% vs 0.84%, blue lines) for $11.3\text{ }\mu\text{g}_{\text{Pt}}\text{ cm}^{-2}$, at 0.3 V vs RHE, and $\Delta = 2.3\%$ (3.64% vs 1.34%, red lines) for $2.3\text{ }\mu\text{g}_{\text{Pt}}\text{ cm}^{-2}$), so does n (i.e., $\Delta = 0.02$ (3.96 and 3.98, blue lines) for $11.3\text{ }\mu\text{g}_{\text{Pt}}\text{ cm}^{-2}$, at 0.3 V vs RHE, and $\Delta = 0.04$ (3.93 and 3.97, red lines) for $2.3\text{ }\mu\text{g}_{\text{Pt}}\text{ cm}^{-2}$). That is, the ORR performance indicators obtained are more influenced by the electrolyte concentration at relatively lower loadings.

Fig. 7 shows the similar comparison in different KOH solutions, for Printex carbon and Graphene, with a representative catalyst loading of 90.8 $\mu\text{g cm}^{-2}$. Again, the curves obtained in 1 M KOH have the same shape as those obtained in 0.1 M KOH. Clearly, the higher electrolyte concentration, the larger disk potential range is for H_2O_2 generation. Also, with increasing the KOH concentration, the ORR performance indicators follow the same trend observed for Pt/C. Taking $\%H_2O_2$ as an example, there is $\Delta = 13\%$ (47% vs 60%, black lines) for Printex, at 0.3 V vs RHE, and $\Delta = 4\%$ (54% vs 58%, red lines) for graphene. More difference can be seen with more negative disk potentials. In addition, the difference between the $\%H_2O_2$ electrogenerated from Printex carbon and graphene is lower in 1 M KOH than in 0.1 M KOH, and so does n .

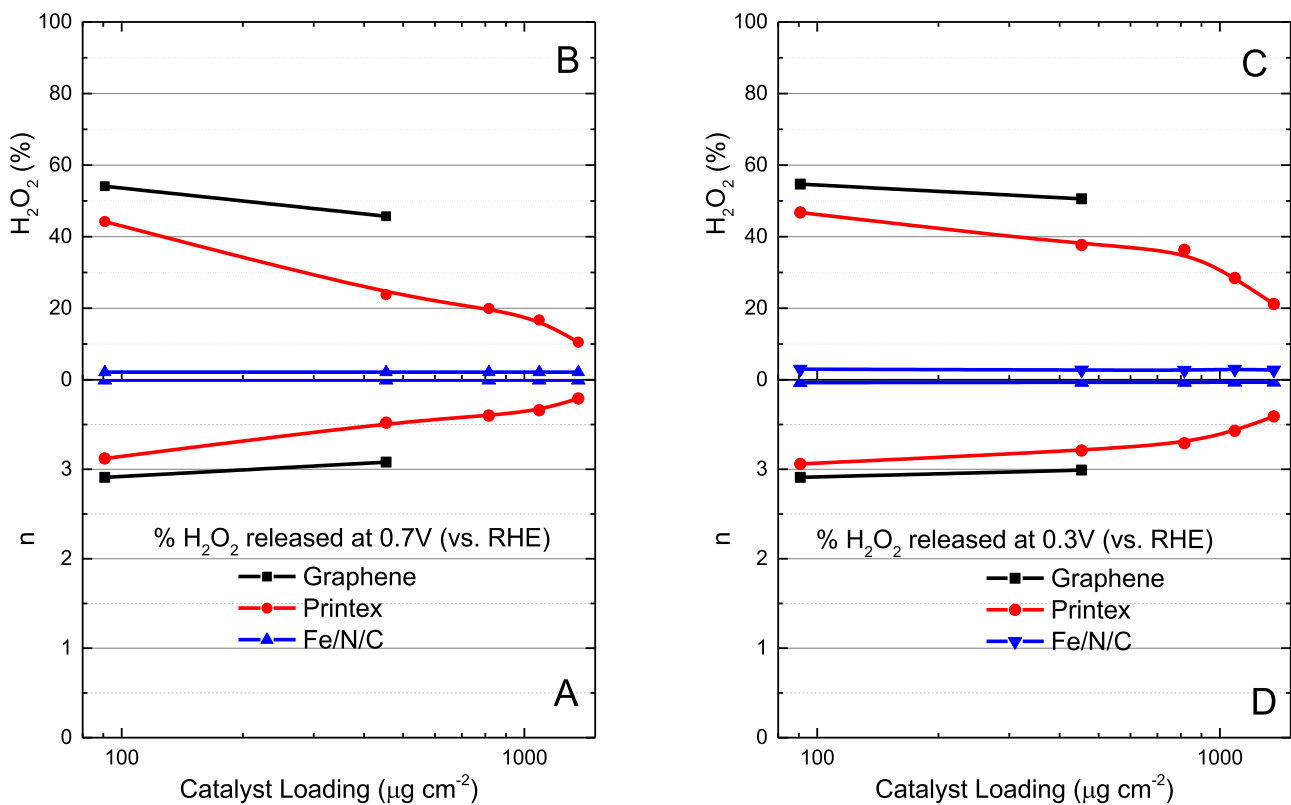


Fig. 10. Variation of the selectivity (%H₂O₂) and the number of electron transferred, under different disk potentials (A) 0.7 V and (B) 0.3 V vs RHE, at 1600 rpm in 0.1 M KOH solution, for metal free catalysts (Printex, graphene) and non-noble metal catalysts (Fe/N/C), as a function of the catalyst loading on RRDE. (For interpretation of the references to colour in this figure legend, the reader is referred to the web version of this article.)

Fig. 8 shows the case of MOF-based Fe/N/C. These results are quite consistent with those of Pt/C, Printex carbon and graphene catalysts. It is worth to point out that again low catalyst loadings (e.g., 90.8 vs 817.1 µg cm⁻²) are more sensitive to the electrolyte concentration in terms of %H₂O₂ and *n* than high loadings. In addition, in the ORR curve of 817.1 µg cm⁻² in 1 M KOH a sharp current spike appears at 0.887 V vs RHE before it plateaued at the diffusion-limited current density; while for the curves obtained in 0.1 M KOH that spike shows up only for higher catalyst loading (e.g., 1089.5 µg cm⁻² rather than 817.1 µg cm⁻²). This is due to the low O₂ solubility in the more concentrated KOH solution, resulting in a longer time for oxygen to diffuse and to reach all the catalyst active sites.

3.5. Summary on the %H₂O₂ and *n* vs. catalyst loading

Considering the catalysts have similar catalytic trend in both 0.1 M and 1 M KOH solutions, herein, we take 0.1 M KOH solution as an example to summarize the trends found for %H₂O₂ and *n* with the catalyst loading. Fig. 9 shows the curves of %H₂O₂ and *n* of 20 wt% Pt/C catalyst, as a function of the catalyst loading on RRDE (via a logarithmic scale), under different disk potentials. Obviously, at each disk potential, the magnitude of the variations of %H₂O₂ and *n* decreased, with increasing the catalyst loading. On the other hand, at the same catalyst loading, a lower disk current corresponds to a lower *n* and higher %H₂O₂. Further, with increasing the catalyst loading, this variation decreases.

Fig. 10 shows the variation of %H₂O₂ and *n*, under two different disk potentials (0.3 and 0.7 V vs RHE), for metal free catalysts (Printex, graphene) and non-noble metal catalysts (Fe/N/C), as a function of the catalyst loading on RRDE. Similar trend can be seen, i.e., with increasing the catalyst loading, %H₂O₂ decreased and *n*

increased. The Printex and graphene show the obvious variation, while the Fe/N/C catalyst does not; this is due to the former ones are not active and more related to 2 e⁻ transfer, while the latter are quite active and shows obvious 4 e⁻ transfer.

4. Conclusions

In this work, we have systematically investigated the catalyst loading effect on ORR performance including activity, diffusion-limited current density, %H₂O₂ and *n*, in alkaline solutions (0.1 M and 1 M KOH), by RRDE. Four types of representative catalysts including noble metal, metal-free and non-noble metal catalysts were selected to make the measurements. The main findings could be summarized as the following:

- 1) The catalyst ORR performance is indeed affected by the catalyst loading on the electrode. Therefore, for a new catalyst, it is highly recommended to study the catalyst loading effect in order to fully understand its electrochemical properties.
- 2) The optimum loading range is such that allows the full coverage of the electrode substrate, but is as low as possible to avoid a too thick catalyst layer, to maximize the catalyst utilization and to avoid the underestimation of the electrogenerated H₂O₂.
- 3) Generally, with increasing catalyst loading, the ORR activity increases, and the %H₂O₂ decreases. In order to make a better comparison between different research groups, the catalyst loading ranges for different types of catalyst are suggested in this work, such as for 20 wt% Pt/C catalyst with the loading range of 10–20 µg_{Pt} cm⁻², while for metal-free and non-noble metal catalysts with a loading range of 100–800 µg cm⁻², depending on the physical chemical properties (surface composition, textural properties and specific surface area) of the catalyst.

4) For the catalysts that follow a direct four-electron pathway such as Pt/C and Fe/N/C reported here, in a certain loading range, the values of limiting current density, %H₂O₂ and *n* are not significantly affected by the catalyst loadings. On the other hand, due to their intrinsic catalytic activity and specific surface area, the performance indicators of metal free catalysts (Printex and graphene) that follow a “2e[−] + 2e[−]” pathway are more affected by the catalyst loading than those of catalysts with 4e[−] transfer process.

5) Thinner catalyst layer (active sites sparsely distributed on the electrode surface) “promotes” the H₂O₂ production, and sometimes the theoretical diffusion-limited current density for a four-electron pathway could not even be reached. On the other hand, a thicker catalyst layer limits the escape of H₂O₂ to be caught by Pt ring (due to the internal diffusion in catalyst layer), resulting in a slightly decreased H₂O₂ production; in addition, the non-uniform surface may also bring signal waves in the polarization curves.

6) The catalysts kept similar ORR behaviours in KOH solutions with different concentrations. However, with a higher concentration, the diffusion-limited current density decreased, the %H₂O₂ increased and *n* decreased. In addition, the values of these indicators were less in 1 M KOH than in 0.1 M KOH.

7) The impact of the electrolyte concentration (e.g., 1 M and 0.1 M KOH) on the ORR performance indicators is higher at relatively lower catalyst loadings.

Acknowledgments

This work was financially supported by the *Fonds de Recherche du Québec-Nature et Technologies* (FRQNT), the Natural Sciences and Engineering Research Council of Canada (NSERC), *Institut National de la Recherche Scientifique* (INRS), and *Centre Québécois sur les Matériaux Fonctionnels* (CQMF). Q. Wei and X. Yang gratefully acknowledge the scholarship from China Scholarship Council (CSC) and FRQNT.

Appendix A. Supplementary data

Supplementary data associated with this article can be found, in the online version, at <http://dx.doi.org/10.1016/j.apcatb.2017.01.001>.

References

- [1] C. Song, J. Zhang, in: J. Zhang (Ed.), *PEM Fuel Cell Electrocatalysts and Catalyst Layers*, Springer, London, 2008, pp. 89–134.
- [2] Y. Jiao, Y. Zheng, M. Jaroniec, S.Z. Qiao, *J. Am. Chem. Soc.* 136 (2014) 4394–4403.
- [3] M. Shao, Q. Chang, J.-P. Dodelet, R. Chenitz, *Chem. Rev.* 116 (2016) 3594–3657.
- [4] J. Liu, E. Li, M. Ruan, P. Song, W. Xu, *Catalysts* 5 (2015) 1167–1192.
- [5] S. Sun, F. Jaouen, J.-P. Dodelet, *Adv. Mater.* 20 (2008) 3900–3904.
- [6] S. Sun, G. Zhang, D. Geng, Y. Chen, R. Li, M. Cai, X. Sun, *Angew. Chem. Int. Ed.* 50 (2011) 422–426.
- [7] G. Zhang, R. Chenitz, M. Lefèvre, S. Sun, J.-P. Dodelet, *Nano Energy* (2016), <http://dx.doi.org/10.1016/j.nanoen.2016.02.038>.
- [8] M.A. Rahman, X. Wang, C. Wen, *J. Electrochem. Soc.* 160 (2013) A1759–A1771.
- [9] V. Caramia, B. Bozzini, *Mater. Renew. Sustain. Energy* 3 (2014) 1–12.
- [10] F. Cheng, J. Chen, *Chem. Soc. Rev.* 41 (2012) 2172.
- [11] J.-S. Lee, S.T. Kim, R. Cao, N.-S. Choi, M. Liu, K.T. Lee, J. Cho, *Adv. Energy Mater.* 1 (2011) 34–50.
- [12] Y. Li, H. Dai, *Chem. Soc. Rev.* 43 (2014) 5257–5275.
- [13] M.H.M.T. Assumpção, R.F.B. De Souza, D.C. Rascio, J.C.M. Silva, M.L. Calegaro, I. Gaubeur, T.R.L.C. Paixão, P. Hammer, M.R.V. Lanza, M.C. Santos, *Carbon* 49 (2011) 2842–2851.
- [14] M.H.M.T. Assumpção, A. Moraes, R.F.B. De Souza, I. Gaubeur, R.T.S. Oliveira, V.S. Antonin, G.R.P. Malpass, R.S. Rochad, M.L. Calegaro, M.R.V. Lanzad, M.C. Santos, *Appl. Catal. Gen.* 411–412 (2012) 1–6.
- [15] N. Guillet, L. Roué, S. Marcotte, D. Villers, J.P. Dodelet, N. Chhim, S. Tré Vin, J. *Appl. Electrochem.* 36 (2006) 863–870.
- [16] T. Poux, F.S. Napskiy, T. Dintzer, G. Kéranguéven, S. Ya Istomin, G.A. Tsirlina, E.V. Antipov, E.R. Savinov, *Catal. Today* 189 (2012) 83–92.
- [17] J. Healy, C. Hayden, T. Xie, K. Olson, R. Waldo, M. Brundage, H. Gasteiger, J. Abbott, *Fuel Cells* 5 (2005) 302–308.
- [18] D.A. Schiraldi, *J. Macromol. Sci. Part C* 46 (2006) 315–327.
- [19] S.J. Hamrock, M.A. Yandrasits, *J. Macromol. Sci. Part C* 46 (2006) 219–244.
- [20] Jose M. Campos-Martin, G. Blanco-Brieva, *Angew. Chem. Int. Ed.* 45 (2007) 6962–6984.
- [21] A. Bonakdarpour, Daniel Esau, Hillary Cheng, Andrew Wang, Elöd Gyenge, David P. Wilkinson, *Electrochim. Acta* 56 (2011) 9074–9081.
- [22] J. García-Serna, T. Moreno, P. Biasi, M.J. Cocco, J.-P. Mikkola, T.O. Salmi, *Green Chem.* 16 (2014) 2320.
- [23] I. Yamamoto, T. Onizawa, S. Takenaka, K. Otsuka, *Angew. Chem. Int. Ed.* 42 (2003) 3653–3655.
- [24] W.R.P. Barros, T. Ereno, A.C. Tavares, M.R.V. Lanza, *ChemElectroChem* 5 (2015) 714–719.
- [25] W.R.P. Barros, Q. Wei, G. Zhang, S. Sun, M.R.V. Lanza, A.C. Tavares, *Electrochim. Acta* 162 (2015) 263–270.
- [26] G. Tamizhmani, J.-P. Dodelet, D. Guay, L. Dignard-Bailey, *J. Electroanal. Chem.* 444 (1998) 121–125.
- [27] E. Farjami, L.J. Deiner, *J. Electrochem. Soc.* 162 (2015) H571–H578.
- [28] N. Ramaswamy, S. Mukerjee, *J. Phys. Chem. C* 115 (2011) 18015–18026.
- [29] H. Peng, Z. Mo, S. Liao, H. Liang, L. Yang, F. Luo, H. Song, Y. Zhong, B. Zhang, *Sci. Rep.* 3 (2013) 1765.
- [30] W.E. Mustain, J. Prakash, *J. Power Sources* 170 (2007) 28–37.
- [31] S. Marcotte, D. Villers, N. Guillet, L. Roué, J.-P. Dodelet, *Electrochim. Acta* 50 (2004) 179–188.
- [32] M. Lefèvre, J.-P. Dodelet, *Electrochim. Acta* 48 (2003) 2749–2760.
- [33] R. Zhou, Y. Zheng, M. Jaroniec, S.-Z. Qiao, *ACS Catal.* 6 (2016) 4720–4728.
- [34] A. Bonakdarpour, M. Lefèvre, R. Yang, F. Jaouen, T. Dahn, J.-P. Dodelet, J.R. Dahn, *Electrochim. Solid-State Lett.* 11 (2008) B105–B108.
- [35] A. Bonakdarpour, C. Delacote, R. Yang, A. Wieckowski, J.R. Dahn, *Electrochim. Commun.* 10 (2008) 611–615.
- [36] A. Bonakdarpour, T.R. Dahn, R.T. Atanasoski, M.K. Debe, J.R. Dahn, *Electrochim. Solid-State Lett.* 11 (2008) B208–B211.
- [37] X. Li, H.-J. Zhang, H. Li, C. Deng, J. Yang, *ECS Electrochem. Lett.* 3 (2014) H33–H37.
- [38] Y.-H. Shih, G.V. Sagar, S.D. Lin, *J. Phys. Chem. C* 112 (2008) 123–130.
- [39] M. Bron, S. Fiechter, P. Bogdanoff, H. Tributsch, *Fuel Cells* 2 (2002) 137–142.
- [40] E. Proietti, F. Jaouen, M. Lefèvre, N. Larouche, J. Tian, J. Herranz, J.-P. Dodelet, *Nat. Commun.* 2 (2011) 416.
- [41] G. Wu, K.L. More, C.M. Johnston, P. Zelenay, *Science* 332 (2011) 443–447.
- [42] T. Shinagawa, A.T. Garcia-Esparza, K. Takanabe, *Sci. Rep.* 5 (2015).
- [43] H. Li, H. Liu, Z. Jong, W. Qu, D. Geng, X. Sun, H. Wang, et al., *Int. J. Hydrogen Energy* 36 (2011) 2258–2265.
- [44] J. Qiao, L. Xu, L. Ding, P. Shi, L. Zhang, R. Baker, J. Zhang, *Int. J. Electrochem. Sci.* 8 (2013) 1189–1208.
- [45] R.E. Davis, G.L. Horvath, C.W. Tobias, *Electrochim. Acta* 12 (1967) 287–297.